Molecular Simulation

Wetting transition of nanodroplets of water on textured surfaces: a molecular dynamics study

Sandip Khan[a] & Jayant K. Singh[a]

[a] Department of Chemical Engineering, Indian Institute of Technology Kanpur, Kanpur, 208016India
Published online: 24 Jul 2013.

PLEASE SCROLL DOWN FOR ARTICLE

Taylor & Francis
Taylor & Francis Group

Wetting transition of nanodroplets of water on textured surfaces: a molecular dynamics study

Sandip Khan and Jayant K. Singh*

Department of Chemical Engineering, Indian Institute of Technology Kanpur, Kanpur 208016, India

The crossover behaviour of water droplet's state from the Wenzel state to the Cassie state with varying pillar height and surface fraction is examined critically using molecular dynamics. We report the effect of the system size on the wetting behaviour of water droplets by examining the contact angle for both regimes. We observe that when the droplet size is comparable to the pillar dimension, the contact angle of droplets fluctuates with increasing droplet size because of the contact line pinning, which is more pronounced in the Wenzel regime. We further demonstrate the phantom-wall method to evaluate free energy of intermediate wetting states.

Keywords: wetting transition; nanodroplet; rough surfaces; molecular dynamics

1. Introduction

Superhydrophobic surfaces are frequently observed in nature, especially on plants [1,2] and insects.[3] These surfaces possess a microscale/nanoscale hierarchical structure and are characterised by a large contact angle and a small sliding angle. The development of patterned surfaces has recently gained attention because of their potential applications in anti-icing,[4] superoleophobic [5] and antifouling [6] surfaces, among other applications. It is well-known that the superhydrophobicity of a surface is mainly due to its low surface energy, which can be controlled by manipulating the nature of the surface topography through chemical or physical modifications. [7] With the advent of microfabrication techniques, it has become possible to control the chemical or topographical patterning of a substrate on micrometer length scales, and thus various controlled surfaces can be used in micro- or nanoscale devices. The fluid behaviour at the vicinity of the surface is greatly influenced by the nature of the surface, and surface tension plays an important role in the structure and dynamics of the fluid.[8] Numerous textured structures have been reported to effectively enhance the hydrophobicity of a solid surface, but so far there has been only limited research on how shapes and dimensions of the texture enhance surface hydrophobicity.[9,10] Towards this goal, molecular simulation can provide a fundamental understanding of the mechanism from a molecular point of view and can be used to explore the interfacial properties for practical purposes.[11–19]

Wetting on rough surfaces can be explained by either the Wenzel [20] or the Cassie [21] model. In the Wenzel model, it is assumed that the water droplet penetrates the surface texture, which makes the interface homogenous.

The apparent contact angle is described by

$$\cos \theta_r^w = r \cos \theta_e \tag{1}$$

where the roughness parameter r is the ratio of the actual surface area of the rough surface to the projected surface area, and θ_e is the intrinsic contact angle on the flat surface. According to the Wenzel model, the hydrophilicity or hydrophobicity of a substrate is amplified by increases in surface roughness. On the other hand, when a water droplet forms a heterogeneous composite interface with air trapped in the grooves of the surface, the apparent contact angle is given as

$$\cos \theta_r^c = f \cos \theta_e + f - 1 \tag{2}$$

where f is the surface fraction of the solid–liquid interface at the base of the droplet. However, the equilibrium state (Wenzel or Cassie) of the droplet depends on the nature of the rough surface. Numerous attempts have been made to distinguish these two states through dimensional descriptions of the rough surface.[22–27] For example, the transition from the Wenzel state to the Cassie state has been observed using different approaches, such as by manipulating the hole dimensions (hole diameter, hole depth and hole interval) of a porous alumina surface,[25] by adding silica nanoparticles on a silica surface to enhance the surface roughness at a constant surface fraction [26] or by varying the dimensions of the micropillars on a polydimethylsiloxane (PDMS) surface [24] or on a silicon surface.[27] Furthermore, whether a droplet will be in a Cassie or Wenzel state can also be controlled though the alignment of carbon nanotubes on the surface.[28] However, in some cases, both states can be found on the same patterned surface, depending on the

*Corresponding author. Email: jayantks@iitk.ac.in

way the liquid droplet is placed on the surface.[29,30] For such cases, the contact angle hysteresis of a droplet in the Wenzel state is very large compared to that in the Cassie state because of the pinning of the contact line.[16,31] In addition to the surface modifications, the transition between the Cassie and the Wenzel states can also be observed by applying an external field,[32,33] vertical vibration,[34,35] heating,[36] external force [14,30] or pressure.[37] It has been shown that the transition from the Cassie to the Wenzel state may involve an intermediate wetting regime such as a mushroom-like state or Cassie impregnation.[38–40] However, the Wenzel state is more energetically favourable than the Cassie state.[30,41] The free energy difference between these two states can be computed using various techniques.[30,40,42–45] For example, Koishi et al. [30] used molecular dynamics 'raining' method where the probability of a nanodroplet transitioning to the wetted state at different impact velocities was used to find the free energy barrier between the two wetting states. However, such method is now known to have limited accuracy.[46] On the other hand, Giacomello et al. [47] used restrained molecular dynamics-parallel tempering to evaluate the free-energy barrier between the two states. They note that rare-event sampling techniques are necessary to simulate the transition events due to the large free energy barrier (> 10 kT). Savoy and Escabedo [46] have recently extended the boxed molecular dynamics method to study the free-energy landscape of wetting states. Recently, Kumar et al. [40] estimated the free energies of different wetting states for a Lennard-Jones (LJ) system using grand canonical Monte Carlo simulation. On the other hand, Leroy et al. [45] demonstrated a phantom-wall method for calculating the free energies of different wetting states with respect to that of a droplet on a smooth surface. In particular, they have looked into various possible scenarios of defects on the top layer of the graphite surface, and by doing so they have varied the roughness in terms of contour length of the defects. In the other case, [48] they have looked at the surface heterogeneity with different heights of the pillars. They reported that the

water-surface free energy increases either with contour length or surface heterogeneity. However, it is not clear how the nanodrop behaves without imposing any states under static conditions, and in general how the contact angle changes with surface heterogeneity. Further, it is not clear how the system size and initial configuration affect the contact angle and wetting states. To address these questions, we examine the behaviour of water droplets on pillared surfaces with varying surface fractions and roughness factors. In addition, we examine the effect of the system size using molecular dynamics. We explore many different wetting states that can exist on the same surface, including the Cassie state, partial Wenzel or mushroom-like states and the full Wenzel state, by manipulating the surface–fluid interaction. In addition, the phantom-wall method [49] is demonstrated to evaluate the free energies of different wetting states. The rest of this chapter is organised as follows. Section 2 describes the model and methods employed in this work. Section 3 presents the results and discussion, followed by our conclusion in Section 4.

2. Model and methodology

2.1 Model

Molecular dynamic simulations are carried out under constant number of particles N, volume V and the temperature T (NVT ensemble) using DLPOLY [50] package. All simulations are conducted at temperature $T = 300$ K. The building block of pillared surfaces consists of a base layer and a pillar, in which carbon atoms are separated by 1.53 Å, and the distance between adjacent layers is 3.4 Å. The dimension of the base layer and the pillar depends on roughness factor r and surface fraction f of the pillared surface as shown in Figure 1. Surface fraction and roughness factor are calculated from the projected area of the pillar (S_a), area of the base layer (S_b) and the area of the sidewall of a pillar (S_c) as given by the following relation.
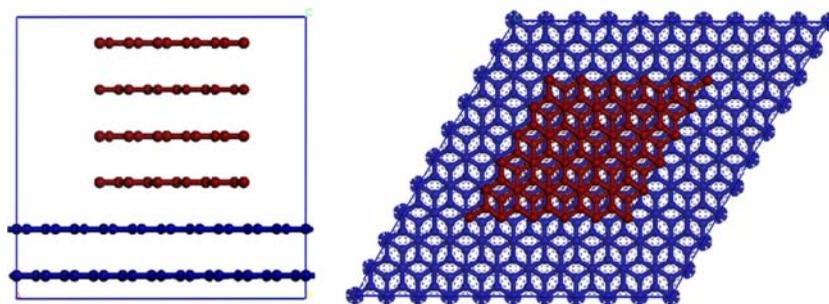

Figure 1.   Side and top views of a building block of the pillared surface.

$$f = \frac{S_a}{S_b}, \quad r = \frac{S_b + 4 \times S_c}{S_b} \qquad (3)$$

In this study, we consider three different surface fractions $f = 0.25$, 0.39 and 0.51 with varying roughness factor in the range $1.31-3.55$, $1.5-5.00$ and $1.65-6.21$, respectively. Pillar height, h, is varied from 1 atomic layer to 8 atomic layers of graphene sheets for each f. Pillar width is kept constant at 12.3 Å. The surface is kept fixed at the bottom of the simulation box during all the simulations. The lateral dimension of the simulation box is kept same as that of the surface and is varied from 150 $\times$ 150 to 200×200 Å^2 depending on the size of the droplet. The height of the simulation box is taken as 300 Å to avoid any interaction of periodic images of the droplet. Periodic boundary condition is applied in the all directions.

Water–water interaction is described by the SPC/E [51] model in which hydrogen atoms are located at 1 Å from the oxygen atom with an H–O–H angle of 109.47°. Bond distance and bond angle are fixed throughout the simulation with SHAKE algorithm.[52] The intermolecular interaction is defined as follows:

$$U(r_{ij}) = 4\varepsilon \left[\left(\frac{\sigma}{r_{ij}} \right)^{12} - \left(\frac{\sigma}{r_{ij}} \right)^6 \right] + \sum_{i=1}^{3} \sum_{j=1}^{3} \frac{q_i q_j}{r_{ij}} \qquad (4)$$

where r_{ij} is the distance between any pair of atoms i and j, σ represents the atom size, ε is the interaction energy depth between two atoms and q_i and q_j are the charges centred on the individual atoms of different water molecules. In this water model, the LJ interaction is considered for oxygen atom only. Carbon–carbon interaction is taken from Werder et al. [53] Surface–water interaction is represented by LJ potential and the corresponding interaction parameters are calculated using the Lorentz-Berthelot mixing rules: $\sigma_{ij} = (\sigma_i + \sigma_j)/2$ and $\varepsilon_{ij} = \sqrt{\varepsilon_i \varepsilon_j}$. A cut-off radius of 10 Å is used for LJ and electrostatic interactions. Electrostatic interactions are incorporated using the single particle mesh Ewald method. [54] About $2000-5000$ water molecules in a cubic lattice are placed on a graphite surface for generating the initial configuration. Each simulation is carried out for 2 ns with an integration time step of 2 fs in which last 200 ps is used to average over different structural and dynamical properties. The Nosé–Hoover thermostat is used to maintain the system temperature with a relaxation constant of 1.0 ps.

2.2 Methodology

Graphical binning approach is considered to calculate various properties such as vapour–liquid densities and contact angle. In this approach, we assume azimuthal symmetry in the droplet and introduce the cylindrical coordinate system (r, z), where r is the distance from z-axis. Such approach was earlier used by Werder et al. [53] and Aluru and co-workers [55]. We have considered the top most surface layer for the zero reference level and the surface normal through the centre of mass of the droplet as the reference axis. The bins have a height of 1 Å and are of equal volume, i.e. the radial bin boundaries are located at $r_i = \sqrt{(i\delta A/\pi)}$ for $i = 1, \ldots, N$ bin with a base area per bin of $\delta A = 95$ Å^2. Once the drop is equilibrated, the configurations are extracted at a certain interval of time during simulation. For each configuration, the location of water molecules is traced based on the position of oxygen atom, and added to its corresponding bin based on the centre of the mass of the droplet. Mean number of the water molecules and its corresponding density is calculated upon averaging 200 configurations. Contact angle is extracted from a two-step procedure from the profiles as described by de Ruijter et al. [56]. First, the location of the equimolar dividing surface is determined within every single horizontal layer of the binned drop. Second, a circular best fit through these points is extrapolated to the surface where the contact angle θ is measured. The boundary between equilibrated liquid and vapour interface for a given droplet is determined at the position where the density is half of bulk water density and is modelled using the relation for liquid–gas interface:

$$\rho(r) = \frac{1}{2}(\rho^{\mathrm{L}} + \rho^{\mathrm{V}}) - \frac{1}{2}(\rho^{\mathrm{L}} - \rho^{\mathrm{V}}) \tan h\left(\frac{2(r - r_{\mathrm{e}})}{d} \right), \quad (5)$$

where, ρ^{L} and ρ^{V} are liquid and vapour densities, respectively, r is the distance from origin to the droplet surface, r_{e} is the centre of the interface region and d is the interface thickness. The points on the equimolar surface below a height of 8 Å from the graphite surface are not taken into account for the fit, to avoid the influence of density fluctuations at the liquid–solid interface.

In this study, we have examined different types of wetting mode, including Cassie and Wenzel states, depending on the surface fraction and the pillar height. In order to determine the stability of the different wetting modes, we have employed thermodynamic integration (TI) to calculate the free energy of different wetting modes with respect to the droplet on the smooth surface. The method requires gradual turning off the pillar interaction with water molecules to transform the pillared surface to the smooth surface. This transformation can easily be implemented by introducing a coupling parameter λ in the LJ interaction between pillar and water molecule where, $\lambda = 0$ represents the smooth surface (reference surface) and $\lambda = 1$ represents the pillared surface (actual surface). Hence, the free energy difference between the droplet on the pillared surface (actual system) and the droplet on the smooth surface (reference system) is given by:

$$\Delta F = \int_0^1 \left\langle \frac{\partial U(\lambda)}{\partial \lambda} \right\rangle_{N,V,T} d\lambda \tag{6}$$

where $< \cdots >_\lambda$ corresponds to the ensemble average of the enclosed quantity and U is the potential energy of the system which is a function of λ as follows:

$$U(\lambda) = (1 - \lambda)U_A + \lambda U_B \tag{7}$$

where U_A and U_B are the configuration energy of the reference and the actual system, respectively.

The phantom-wall method [49] is employed in this study to determine the free energy of different wetting modes on pillared surfaces with respect to the smooth surface. A smooth graphite surface is used as a phantom wall. The area of the phantom wall is same as that of the pillared surface and has no interaction with the pillared surface. However, it can interact with the water molecules. The phantom wall is introduced parallel to the pillared surface keeping it way below the surface such that it has no effect on the water dynamics. The phantom wall is then gradually shifted towards the pillared surface. Initially, the phantom wall is out of interaction range of the water molecules and as it is shifted upwards, the water molecules start interacting with the phantom wall. The phantom wall is then gradually passed through the pillared surface and lifts the droplet from the pillared surface. Finally, the phantom wall with equilibrated droplet is outside the interaction range of the pillared surface. TI method is then employed to calculate the free energy change during the transformation. Here, the potential energy of the system is a function of z position of the phantom wall. Details of the phantom-wall method are given elsewhere.[45]

3. Results and discussion

Simulations are performed with an initial configuration in which a water droplet is placed on the top of the pillared surfaces. Typically, it takes $500–600$ ps to reach the equilibrium state; after that, the drop attains its equilibrium position on top of the pillars. To understand the water structure on the solid surface, especially near the surface, we plot the density profiles of the water droplets for different groove-patterned structures of varying surface fractions. Figure 2 presents the density profiles of water on pillared surfaces with varying surface fractions ($f = 0.25$– 1) at a constant pillar height $h = 4$. The equilibrated water droplet is found to stay in the Cassie–Baxter regime for the aforementioned pillared surfaces. The local density shows that fluid layering occurs near the surface with a density much higher than the bulk density at the same temperature, 300 K. The droplet recovers the bulk statistics nearly 8 Å away from the surface at that temperature. This phenomenon is due to the significant influence of the
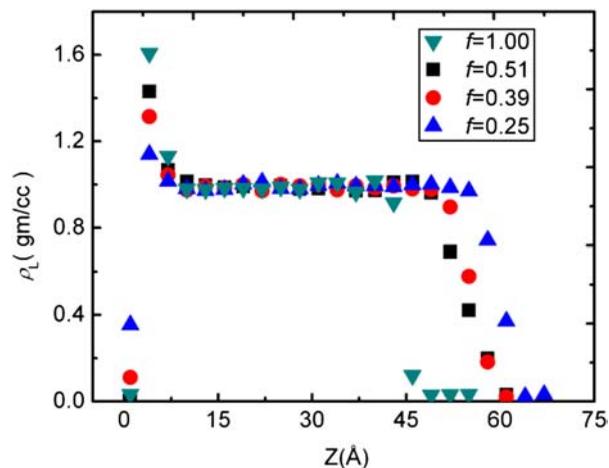

Figure 2.   Z-density profile of a water droplet through centre of mass of the droplet for different surface fractions at $h = 4$.

surface structure on water molecules in the first layer, which may lead to formation of a solid-like structure in the first layer. This was also observed by earlier investigators. [57] The intensity of the first density peak decreases with decreasing surface fraction, due to reduction in energetic contribution of pillars (in this case top layer) with decreasing surface fraction, and water molecules tend to prefer its own kind. As the surface fraction f decreases, the height of the droplet on the surface increases, and the drop is found to be in the Cassie state. However, at $h = 2$ and $f = 0.25$, the droplet is observed to be in the Wenzel state and water molecules readily penetrate the surface texture. The degree of penetration, however, decreases with increasing surface fraction, as illustrated in Figure 3. Interestingly, we do not observe any penetration of water molecules at $f = 0.51$. On the other hand, at the intermediate surface fraction $f = 0.39$, we observe a
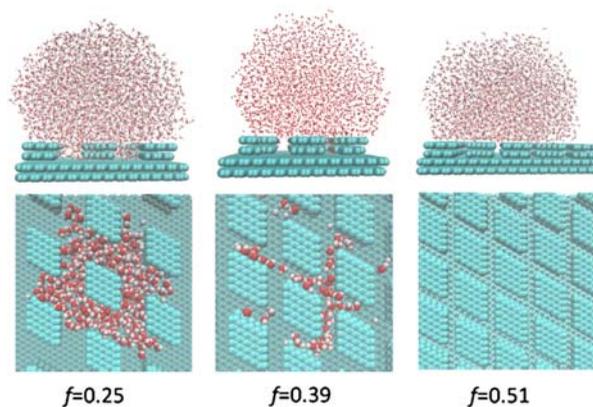

Figure 3.   Configuration snapshots of a water droplet with 4000 water molecules on pillared surfaces (side and top view) for different surface fractions at $h = 2$.

partial Wenzel state. This is in line with the observation of Leroy et al. [48], as seen in their calculation of solid–liquid surface tension which is positive value at high surface fraction or contour length.[45] This indicates that the Cassie state is preferred at large pillar heights or roughness factor. For $h = 2$, the behaviour is similar to that seen for the case of defects on the 1 molecular diameter depth work of Leroy et al. [48]. This clearly states that at higher values of f Wenzel state is thermodynamically unfavourable. A similar observation was also made in an experimental study on rough PDMS surfaces in which the spacing between pillars was changed at a constant pillar height.[58] Therefore, at a lower height, $h = 2$, a transition from the Wenzel state to the Cassie state is observed with increasing surface fraction. On the other hand, at $h = 4$ the water droplet is always in the Cassie state, irrespective of the surface fraction (as studied in this work), as discussed earlier. This observation is also in line with the calculated solid–liquid free energy as a function of surface heterogeneity by earlier workers.[48]

Therefore, a critical pillar height may exist at which the Wenzel state transforms to the Cassie state. Some work in this direction has been done by some workers, and compared the prediction of Wenzel and Cassie–Baxter equations with their simulation data.[18,59] In this work, to investigate the crossover behaviour, we minutely examine the wetting behaviour for each pillar height and rigorously calculate the system size effect, as discussed below, for a surface fraction $f = 0.25$.

To evaluate the critical pillar height at which the Wenzel state transforms to the Cassie state, we vary the pillar height h from 1 to 8. We observe that the water droplet is always in the Wenzel state up to $h = 3$

(corresponding to a roughness factor $r = 1.95$). Upon further increase in pillar height, the water droplet state transforms to the Cassie state. The crossover behaviour of the water droplet from the Wenzel state to the Cassie state is also found in many experimental studies.[25–27,60] For example, Yeh et al. [27] have examined the crossover behaviour of a water droplet on pillar-like patterned surfaces (silicon wafer) at $f = 0.25$ with varying pillar heights, and the roughness factor associated with this transformation was found to be 1.35. On the other hand, Yoshimitsu et al. [60] have found a transition roughness factor of $r \approx 1.2$ for $f = 0.11$ and 0.36; however, the theoretical predictions for the transition roughness factors for these surface fractions are 2.3 and 1.9, respectively.[61] Recently, molecular dynamics simulations were performed for $f = 0.25$ but with different pillar dimensions, [30,62] and the transition roughness factor was found to be around 1.8–2.0, which is also in line with our results.

The wetting behaviour of a water droplet on a pillared surface is greatly influenced by the sharp corner of the pillar when the size of the surface texture is comparable with the droplet size.[18] To study the system size effect on a textured surface, we performed a series of simulations with varying droplet sizes from 2000 to 5000 water molecules. The corresponding contact angles are shown in Figure 4(a), which clearly exhibit fluctuation with system size. This behaviour is in contrast to that seen for the smooth surface.[12] The fluctuation in the contact angle with increasing number of water molecules is more pronounced at a lower pillar height ($h < 4$), as evident from Figure 4(a). The contact angle is more or less constant for $h \geq 4$. Further, in this regime the contact angle is very close to the value (around 136°) predicted
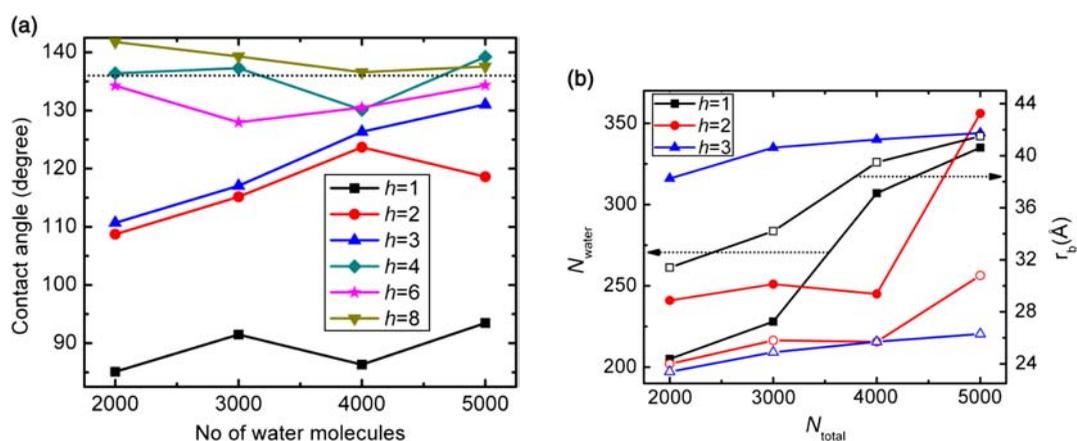
Figure 4.   (Colour online) (a) Contact angle variation as a function of number of water molecules, at $f = 0.25$, for different pillar heights, $h = 1–8$. Dotted line represents the contact angle value predicted by the Cassie–Baxter equation. Errors associated with the contact angles are within 1°. (b) Number of water molecules penetrated into the grooves of the pillared surface and radius of the base layer (first layer from the top of the pillar) of water droplets as a function of number of water molecules. Left axis represents the number of water molecules (close symbols) penetrated into the grooves and right axis represents the radius of the base layer of water droplets (open symbol). Black, red and blue represent $h = 1$, 2 and 3, respectively.

using the Cassie–Baxter equation. However, at a lower pillar height ($h < 4$), where the droplet penetrates the groves of the textured surface, the Wenzel equation does not hold and the contact angle varies significantly with increasing number of water molecules. This was also observed in most experimental studies.[63] Metastable states leading to contact angle hysteresis were predicted long ago by Dettre and Johnson [64]. It should be noted that contact angle of water drop for smooth graphite surface is around 83° as investigated in our earlier work. [12] For $h = 1$, the change in contact angle with an increasing number of water molecules is oscillatory in nature, whereas for $h = 3$, the contact angle continues to increase with increasing number of water molecules.

In order to understand the aforementioned behaviour of the contact angle, we study the nature of contact line of the base layer (first layer at the top of pillar) and the degree of penetration. Water molecules within the groove experience a stronger effectively interaction compared to that on the top of the pillar. This is due to the increase in the number of carbon particles around a water molecule in the groove. The degree of penetration is not uniform though. For example, at a lower pillar height $h = 1$, the number of the water molecules in the grooves gradually increases with increasing droplet size, while for a pillar height $h = 3$ the degree of penetration of the water droplet remains more or less constant for different droplet sizes. Thus, for $h = 3$, spreading of the water droplet is hindered by the surface texture, which results in a continuous increase in the contact angle with increasing system size. Further, beyond $h = 3$, the behaviour is more or less similar to that seen for $h = 3$. The expansion of the base layer of the drop (at the top of the pillar) is also affected by the degree of penetration, as illustrated in Figure 4(b), and results in changing the contact angle with increasing droplet size (for $h < 4$). In addition, the change in the contact angle has a strong dependence on the commensurate–incommensurate wetting of the pillar grooves or contours. This is clearly evident from the snapshots for the pillar heights $h = 1$ and 3, shown in Figure 5. While number of water molecules, N_{water}, increases with increase in the total number of water molecules N_{total}, it is the percentage of water molecules in the grooves which decreases with increasing N_{total}. For example, at $h = 1$ and $N_{total} = 2000$, we observed that 10% of water molecules are in the gooves which decreases to 6.7% for $N_{total} = 5000$. On the other hand, at $h = 3$, the change is from 15.8% to 6.8% with increase in N_{total}, from
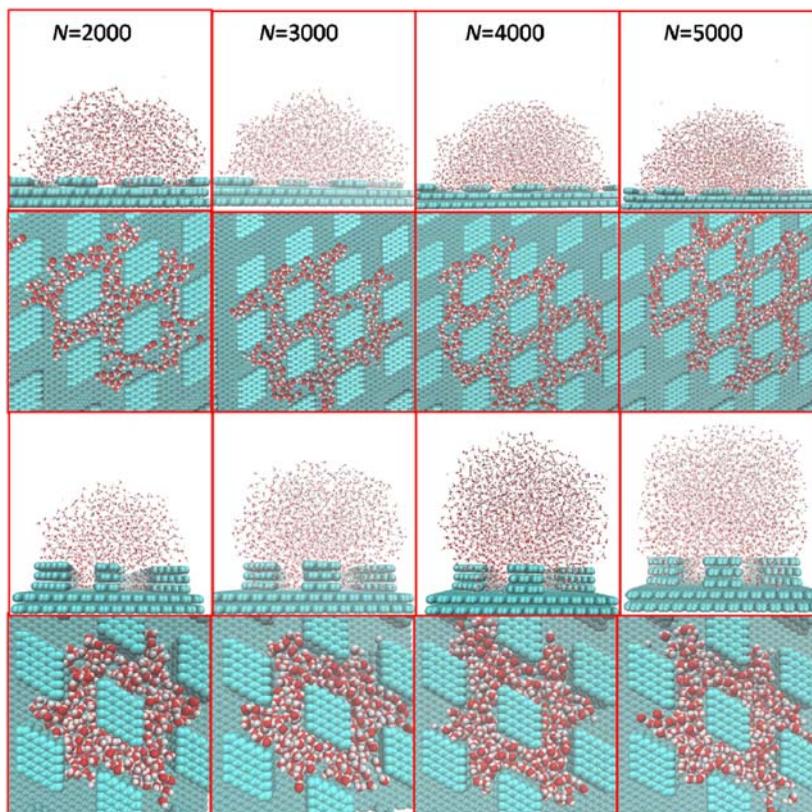

Figure 5.   Configuration snapshots of water droplet on a pillared surface (at the Wenzel state) at $h = 1$ and 3 with increasing droplet size (side and top view). First row represents the side view for $h = 1$. Second row represents the corresponding water molecules in the grooves. Similarly, third and fourth rows are for $h = 3$.
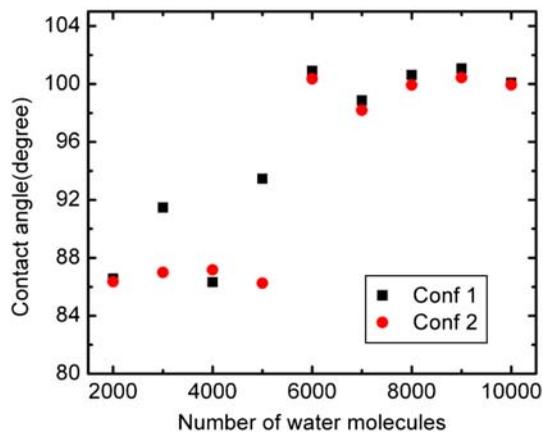
Figure 6. Contact angle variation with increase in number of water molecules due to two different initial configurations. Errors associated with the contact angle are within 1°.

2000 to 5000. While this decrease in percentage of N_{water} is not oscillatory in nature, it is the commensurate–incommensurate wetting of the pillars (see Figure 5) which we found to be the main reason behind oscillatory contact angle. In case of $h = 1$, we noticed that corresponding number of wetted pillars with increasing N_{total} (from 2000 to 5000) are 2, 3, 5 and 5. It should be noted that the drop in the contact angle for $h = 1$ was observed for the case of $N_{total} = 4000$, where we observed a sudden jump in the wetted number of pillars. Further increase in N_{total} to 5000 does not change the number of wetted pillars. On the other hand, for $h = 3$, the number of wetted pillar bases is found not to change with N_{total} (for $2000 \leq N_{total} \leq 5000$). This is clearly in line with the behaviour seen for contact angle or percentage of water in the grooves. The aforementioned study suggests that the spreading of the droplet is hindered by the surface textures, especially in the Wenzel regime; hence, it is expected that there could be several metastable structures. Therefore, the initial drop state (with zero, one, two or more grooves filled) can significantly affect the final structure.

To this end, we study the effect of droplet conditions (initial configurations) and relative dimensions of the droplet size and pillar height at $f = 0.25$. Contact angle of droplets with varying numbers of water molecules is examined from 2000 to 10,000 at an interval of 1000 water molecules. For each system, we create two different initial configurations. In one case, the water droplet is placed on top of the pillar, and in the other case, the surface texture is fully filled with water molecules. These initial configurations are the extreme states for which the final contact angles could differ as a result of the pinning effect. Figure 6 presents the contact angle variation due to different initial configurations. It is apparent that the contact angle of the water droplet strongly depends on the

initial configuration of the droplet up to 5000 water molecules. However, we observe that beyond 5000 water molecules, the contact angle of the water droplet is more or less independent of the initial configuration. Hence, it is evident that there are possibilities of different states depending on drop size, surface texture and conditions imposed on the drop. In order to understand and investigate the stability of the state of the drop, free-energy calculation is required. In the next section, we describe briefly a method which is suitable for such calculations.

3.1   Free-energy calculations

In this section, we present a methodology to evaluate free-energy of a wetting state with respect to a reference state. In order to analyse the transition between the Cassie state to the Wenzel state, we first start from two different initial configurations (see Figure 7) consisting of 3000 water molecules for $f = 0.25$ and $h = 4$. We note that for an initial structure close to the Cassie state, the equilibrated droplet is in the Cassie state, while for an initial structure close to the Wenzel state the equilibrated droplet is in the Wenzel state. This clearly suggests that both states can exist at this surface fraction for $h > 3$ and are separated by some free energy barrier. On the other hand, at lower pillar heights ($h \leq 3$), the water droplet is always in the Wenzel state at $f = 0.25$, irrespective of the initial configuration. We extended this exercise for different surface fractions ($f = 0.39$ and $f = 0.51$), but we did not observe two different states for other surface fractions. Table 1 summarises the different states of the water droplet as a function of surface fraction and pillar height for 2000–5000 water molecules. Here, we re-emphasise that the results presented in this work are in agreement with that of Leroy et al. [45,48], where it is clearly shown, for the Wenzel state, that the free energy increases with height of the pillars.

While various methods exist to evaluate the free energy difference between different wetting states as discussed earlier, we adopt a method based on TI method. The purpose of this section is to demonstrate the phantom-wall method [45,49] to evaluate the free energy change of the system during the transformation between a water droplet on a pillared surface (target system) and a water droplet on a smooth surface (reference system) by changing the surface–water interaction to create an artificial path. In this method, we modulate the pillar–water interaction by introducing a coupling parameter λ that connects the target system ($\lambda = 1$, which represents full interaction between the pillars and the water droplet) to the reference system ($\lambda = 0$, which represents no interaction between the pillars and the water droplet). It should be noted that the drop would not be moving
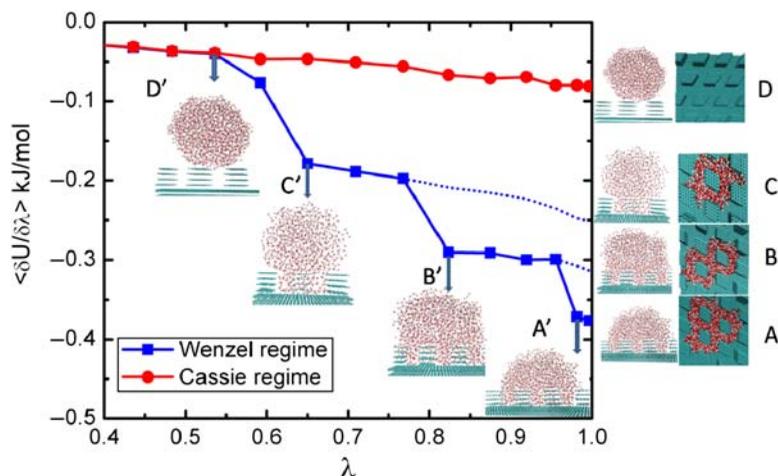
Figure 7.   The free energy change during transformation between the pillared surface and the smooth surface at $f = 0.25$ and $h = 4$. States A, B, C and D represent the different equilibrium structures during transformation. Solid line represents the reverse path ($\lambda = 1–0$) and dotted line represents the forward path. States A′, B′, C′ and D′ represent intermediate structures during transformation.

between different wetting states on the same surface, as the interaction of the surface is being modified. Since our interest is to understand the free energy difference between the Cassie and different Wenzel states, we create two paths. Path I is designated for the case where the initial state is Cassie, and λ is changed from 1 to 0. Path II is for the case where the initial state is Wenzel. Changing λ from 0 to 1 (or 1 to 0), for case I, does not change the state of the droplet which remains in the Cassie state (represented by path D to D′ in Figure 7). On the other hand, if the initial state is Wenzel, i.e. case II, then the transition from $\lambda = 1$ to 0 encounters few metastable states as clearly seen in Figure 7 (A $\rightarrow$ D′). Eventually at a λ earlier than 0, the drop approaches the Cassie state. The two paths clearly indicate that there are many possible states feasible on pillared surface at nanoscale.

Figure 7 also shows the energy derivatives ($\delta U/\delta\lambda$) at different λ values for both paths (represented by solid lines in Figure 7). The difference in ($\delta U/\delta\lambda$) between these two paths decreases as the target systems approach the reference system, and vanishes at a certain λ value ($\lambda = 0.54$), where the droplet is in the Cassie state for both cases. This suggests that for the path A $\rightarrow$ D′ (case II), where the droplet is initially in the Wenzel state, the droplet transforms to the Cassie state before reaching the reference

system λ. However, the transformation from the Wenzel state to the Cassie state is not smooth, as reflected by a few sudden changes in the energy derivative ($\delta U/\delta\lambda$), indicative of phase transition, during the transformation along the path A $\rightarrow$ D′. Hence, we carefully examined each structure associated with the route and found that there are four different structures involved in the transformation, which are designated as states A′, B′, C′ and D′ in Figure 7. We took these structures as the initial configurations for simulations with increasing λ values in order to see the reversibility of the path. We do not see any change in the final configurations at $\lambda = 1$ and the path followed is represented by a dotted line. To this end, we observed (as seen for path A $\rightarrow$ D′) four possible equilibrium structures (three structures are in the Wenzel state and one structure is in the Cassie state) for the surface fraction $f = 0.25$ at $h = 4$. These structures are also seen for a bigger water droplet (consisting of 5000 water molecules). Hence, it is clear that we may observe different possible structures in Wenzel states and some may be metastable. Therefore, it is important to have a mechanism to evaluate the stability of such phases routinely using some free-energy method. In this article, we describe the phantom-wall method, which can be used with much ease in such cases.

Phantom-wall method is a TI and requires a reversible path for the free energy calculation. Initially, a smooth graphite surface with an equilibrated (reference system) droplet is placed as a phantom wall above the pillared surface ($f = 0.25$ and $h = 4$) beyond the cut-off distance between water–pillar interactions, so that initially the water droplet does not interact with the pillared surface. The phantom wall is then shifted gradually towards the pillared surface in increments of 1 Å. As there is no interaction between the phantom wall and the pillared surface, the phantom wall can pass through the pillared

Table 1.   Different wetting states of a water droplet as a function of surface fraction and pillar height.

	$f = 0.25$	$f = 0.39$	$f = 0.51$
$h = 1$	Wenzel	Partial Wenzel	Cassie
$h = 2$	Wenzel	Partial Wenzel	Cassie
$h = 3$	Wenzel	Cassie	Cassie
$h = 4$	Wenzel/Cassie	Cassie	Cassie
$h = 6$	Wenzel/Cassie	Cassie	Cassie

surface, leaving the water droplet on the pillared surface (target system). The initial configuration for each location of the phantom wall is taken from the equilibrated configuration of the previous location. Each simulation is equilibrated for 500 ps to generate an initial configuration for the next simulation. Another 500 ps of simulation is used to equilibrate the system for all locations of the phantom wall, of which the last 200 ps is used to calculate the free energy difference between the target and reference systems. Figure 8 presents a typical configurational energy difference between a wetting state (in this case state A) and the reference state along the thermodynamic path. In the forward path, the phantom wall is shifted downwards from above of the pillared surface, and in the backward path, the phantom wall is shifted upwards from below of the pillared surface. These two paths are completely reversible, as seen in Figure 8. It is noted that the interaction between the phantom wall and the water molecules is same as the interaction between graphite and water molecules (i.e. $\varepsilon_{os} = 0.392$ kJ/mol). Sharp changes in free energy are observed when the phantom wall crosses the top layer and the base layer of the pillared surface. The first sharp change in free energy is due to the droplet transition from the Cassie state to the Wenzel state, and the second sharp change in free energy is due to the droplet entering a specific Wenzel state (here, it is state A). In between, the droplet retains more or less the same structure, which is also reflected in the change in free energy as shown in Figure 8. Therefore, the whole transformation consists of three distinct regimes. In the first regime, the droplet transforms from the Cassie state to the Wenzel state. In the second regime, the droplet is carried through the pillars to the base layer of the pillared surface and in the third regime, the droplet enters Wenzel state A. We also

performed the same exercise for the pillar height $h = 6$ with the same surface fraction, i.e. $f = 0.25$, and observed similar characteristics of the transformation. It is obvious that the phantom wall plays an important role in overcoming the free energy barrier of the transformation in a controlled manner and guides the droplet to a specific, energetically favourable wetting mode, reversibly. Hence, the strength of the phantom wall is an important parameter for controlling the transformation. We extensively studied the system with varying phantom wall strengths, and were able to determine the phantom wall strength necessary to produce each wetting mode (states A, B, C and D). For the case of state C, we create a two-step path. First, we decrease the phantom wall strength from the original graphite–water interaction, $\varepsilon_{os} = 0.392$ kJ/mol (reference system), to $\varepsilon_{os} = 0.20$ kJ/mol (target system) and calculate the configurational energy difference between the target and reference systems at different ε_{os} values. The target system is then used as a reference system for the phantom wall method in the second step. Thus, the free energy of the droplet on the pillared surface with respect to that of the smooth surface will be the summation of the free energy differences evaluated from the two steps. Similarly, for the case of state D, suitable phantom wall strength is found to be 0.1. Thus, by modulating the phantom wall strength, one can control the different wetting modes on the pillared surface, and the free energies of the wetting modes with respect to that of the droplet on a smooth surface can be estimated. We evaluated the free energies of these modes (states A, B, C and D) with respect to that of a droplet on a smooth surface by integrating the energy derivative over the whole transformation and found that the Wenzel regime is more energetically favourable than the Cassie regime. In the Wenzel regime, state C
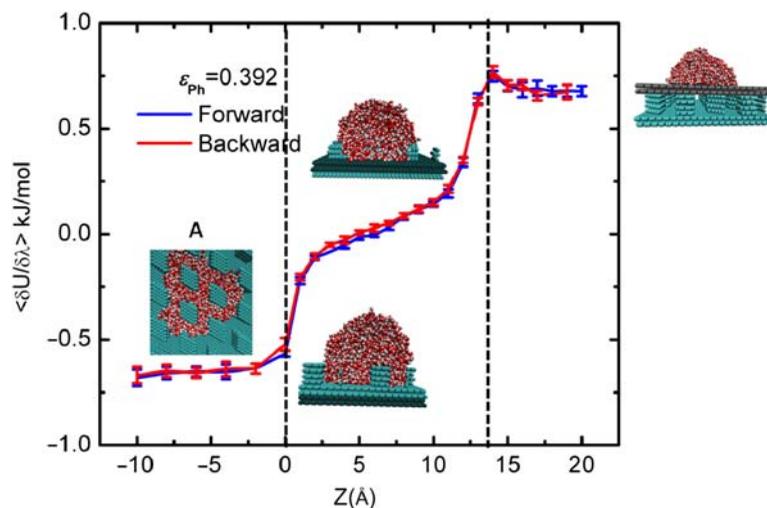

Figure 8. Free energy change for state A during transformation between the pillared surface and the smooth surface at $f = 0.25$ and $h = 4$. Strength of the phantom wall, $\varepsilon_{ph} = 0.392$, is equivalent to that of the smooth graphite–water system.

($\Delta F \approx 0.14$ kJ/mol) is more stable than state A ($\Delta F \approx 0.26$ kJ/mol). The method is relatively simpler to implement, and hence can be easily employed for complex systems as well. It is important to note that the phantom-wall interaction strength evaluated in this work may not be extensible to other systems directly; however, it is expected that it would act as an initial guess. Hence, we believe that this aspect of the work could be important for future studies.

4.   Conclusions

The effect of surface topography on wetting is studied using molecular dynamics simulations. We observed that the Cassie and Wenzel states depend strongly on the surface fraction and pillar height. For a surface fraction $f = 0.51$, we observed that the droplet is in the Cassie state, irrespective of the pillar height as well as the initial configuration. When the spacing between pillars is increased keeping the pillar dimension fixed (i.e. the surface fraction increases), the water droplet penetrates the groves of the pillared surface. For a surface fraction $f = 0.39$, we observed partial Wenzel states up to a pillar height of $h \leq 2$, and beyond this pillar height, $h > 2$, the droplet is always in the Cassie state at this surface fraction. On the other hand, for a surface fraction $f = 0.25$ with a pillar height $h \leq 3$, the water droplet is in the Wenzel state. The current work shows that Wenzel state is unfavourable for higher fraction which is in agreement with recent works. The contact angles for this system ($f = 0.25$ and $h = 1-8$) fluctuate with system size, because of the pinning effect and commensurate–incommensurate wetting of pillar base/grooves, and this fluctuation is more prominent for the Wenzel state. We also examined the effect of the system size on the contact angle for two different configurations (one close to the Cassie state and the other close to the Wenzel state) for a lower pillar height ($h = 1$). We found that the contact angle of the droplet is independent of the initial configuration beyond 5000 water molecules.

We employed TI to calculate the free energies of different wetting states with respect to that of a smooth surface by changing the pillar–water interaction at $h = 4$ for a surface fraction $f = 0.25$. We observed that there are many localised equilibrium structures during the transformation. In this work, we have showed that the phantom-wall method is a novel technique that can be used to calculate the free energies of different wetting modes by modulating the strength of the phantom wall.

Acknowledgements

References

[1] Shirtcliffe NJ, McHale G, Newton I. Learning from super-hydrophobic plants: the use of hydrophilic areas on super-hydrophobic surfaces for droplet control. Langmuir. 2009;25:14121–14128.

[2] Koch K, Bohn HF, Barthlott W. Hierarchically sculptured plant surfaces and superhydrophobicity. Langmuir. 2009;25:14116–14120.

[3] Ding Y, Xu S, Zhang Y, Wang AC, Wang MH, Xiu Y, Wong CP, Wang L. Modifying the anti-wetting property of butterfly wings and water strider legs by atomic layer deposition coating: surface materials versus geometry. Nanotechnology. 2008;19:355708.

[4] Meuler AJ, McKinley GH, Cohen E. Exploiting topographical texture to impart icephobicity. ACS Nano. 2010;4:7048–7052.

[5] Zhao H, Law K-Y, Sambhy V. Fabrication, surface properties, and origin of superoleophobicity for a model textured surface. Langmuir. 2011;27:5927–5935.

[6] Scardino AJ, Zhang H, Cookson DJ, Lamb RN, Nys Rd. The role of nano-roughness in antifouling. Biofouling. 2009;25:757–767.

[7] Wang J, Liu F, Chen H, Chen D. Superhydrophobic behavior achieved from hydrophilic surfaces. Appl Phys Lett. 2009;95:084104.

[8] Assender H, Bliznyuk V, Porfyrakis K. How surface topography relates to materials' properties. Science. 2002;297:973–976.

[9] Yan YY, Gao N, Barthlott W. Mimicking natural superhydrophobic surfaces and grasping the wetting process: a review on recent progress in preparing superhydrophobic surfaces. Adv Colloid Interface Sci. 2011;169:80–105.

[10] Roach P, Shirtcliffe NJ, Newton I. Progress in superhydrophobic surface development. Soft Matter. 2008;4:224–240.

[11] Dai Z-W, Ling J, Huang X-J, Wan L-S, Xu K. Molecular simulation on the interactions of water with polypropylene surfaces. J Phys Chem C. 2011;115:10702.

[12] Dutta RC, Khan S, Singh K. Wetting transition of water on graphite and boron–nitride surfaces: a molecular dynamics study. Fluid Phase Equilibria. 2011;302:310–315.

[13] Dalvi VH, Rossky J. Molecular origins of fluorocarbon hydro-phobicity. Proc Natl Acad Sci. 2010;107:13603.

[14] Koishi T, Yasuoka K, Zeng XC, Fujikawa S. Molecular dynamics simulations of urea–water binary droplets on flat and pillared hydrophobic surfaces. Faraday Discuss. 2010;146:185–193.

[15] Park JH, Aluru R. Temperature-dependent wettability on a titanium dioxide surface. Mol Simul. 2009;35:31–37.

[16] Koishi T, Yasuoka K, Fujikawa S, Zeng C. Measurement of contact-angle hysteresis for droplets on nanopillared surface and in the cassie and wenzel states: a molecular dynamics simulation study. ACS Nano. 2011;5:6834.

[17] Hirvi JT, Pakkanen A. Wetting of nanogrooved polymer surfaces. Langmuir. 2007;23:7724–7729.

[18] Lundgren M, Allan NL, Cosgrove T. Modeling of wetting: a study of nanowetting at rough and heterogeneous surfaces. Langmuir. 2007;23:1187–1194.

[19] Giovambattista N, Debenedetti PG, Rossky J. Effect of surface polarity on water contact angle and interfacial hydration structure. J Phys Chem B. 2007;111:9581.

[20] Wenzel RN. Resistance of solid surfaces to wetting by water. Ind Eng Chem Res. 1936;28:988–994.

[21] Cassie ABD, Baxter S. Wettability of porous surfaces. Trans Faraday Soc. 1944;40:546–551.

[22] Liu B, Lange F. Novel method of producing a superhydrophobic surface on Si. Langmuir. 2010;26:3637–3640.

[23] Bhushan B, Her K. Fabrication of superhydrophobic surfaces with high and low adhesion inspired from rose petal. Langmuir. 2010;26:8207–8217.

[24] Yeo J, Kim S. The effect of the aspect ratio on the hydrophobicity of microstructured polydimethylsiloxane (PDMS) robust surfaces. Microsyst Technol. 2010;16:1457–1463.

[25] Ran C, Ding G, Liu W, Deng Y, Hou W. Wetting on nanoporous alumina surface: transition between Wenzel and Cassie states controlled by surface structure. Langmuir. 2008;24:9952–9955.

[26] Yeh K-Y, Cho K-H, Chen J. Preparation of superhydrophobic surfaces of hierarchical structure of hybrid from nanoparticles and regular pillar-like pattern. Langmuir. 2009;25:14187–14194.

[27] Yeh K-Y, Chen L-J, Chang Y. Contact angle hysteresis on regular pillar-like hydrophobic surfaces. Langmuir. 2008;24:245–251.

[28] Zhang L, Resasco E. Single-walled carbon nanotube pillars: a superhydrophobic surface. Langmuir. 2009;25:4792–4798.

[29] He B, Patankar NA, Lee J. Multiple equilibrium droplet shapes and design criterion for rough hydrophobic surfaces. Langmuir. 2003;19:4999–5003.

[30] Koishi T, Yasuoka K, Fujikawa S, Ebisuzaki T, Zeng C. Coexistence and transition between Cassie and Wenzel state on pillared hydrophobic surface. Proc Natl Acad Sci. 2009;106: 8435–8440.

[31] Lafuma A, Quere D. Superhydrophobic states. Nat Mater. 2003;2:457–460.

[32] Xia J, Wu J. Electrowetting on a dielectric surface roughened with zinc oxide tetrapod nanocrystals. Physica E. 2010;43:81–84.

[33] Manukyan G, Oh JM, Ende DV, Lammertink RGH, Mugele F. Electrical switching of wetting states on superhydrophobic surfaces: a route towards reversible Cassie-to-Wenzel transitions. Phys Rev Lett. 2011;106:014501.

[34] Bormashenko E, Pogreb R, Whyman G, Erlich M. Cassie–Wenzel wetting transition in vibrating drops deposited on rough surfaces: is the dynamic Cassie–Wenzel wetting transition a 2D or 1D affair?. Langmuir. 2007;23:6501–6503.

[35] Jonas A, Karadag Y, Tasaltin N, Kucukkara I, Kiraz A. Probing microscopic wetting properties of superhydrophobic surfaces by vibrated micrometer-sized droplets. Langmuir. 2011;27: 2150–2154.

[36] Liu G, Fu L, Rode AV, Craig SJ. Water droplet motion control on superhydrophobic surfaces: exploiting the Wenzel-to-Cassie transition. Langmuir. 2011;27:2595–2600.

[37] Deng T, Varanasi KK, Hsu M, Bhate N, Keimel C, Stein J, Blohm M. Nonwetting of impinging droplets on textured surfaces. Appl Phys Lett. 2009;94:133109.

[38] Ishino C, Okumura K. Wetting transitions on textured hydrophilic surfaces. Eur Phys J E. 2008;25:415–424.

[39] Boreyko JB, Baker CH, Poley CR, Chen H. Wetting and dewetting transitions on hierarchical superhydrophobic surfaces. Langmuir. 2011;27:7502–7509.

[40] Kumar V, Sridhar S, Errington R. Monte Carlo simulation strategies for computing the wetting properties of fluids at geometrically rough surfaces. J Chem Phys. 2011;135:184702.

[41] Nosonovsky M, Bhushan B. Patterned nonadhesive surfaces: superhydrophobicity and wetting regime transitions. Langmuir. 2008;24:1525–1533.

[42] Cui XS, Li W. On the possibility of superhydrophobic behavior for hydrophilic materials. J Colloid Interface Sci. 2010;347:156–162.

[43] Gross M, Varnik F, Raabe D, Steinbach I. Small droplets on superhydrophobic substrates. Phys Rev E. 2010;81:051606.

[44] Liu HH, Zhang HY, Li W. Thermodynamic analysis on wetting behavior of hierarchical structured superhydrophobic surfaces. Langmuir. 2011;27:6260–6267.

[45] Leroy F, Muller-Plathe F. Rationalization of the behavior of solid– liquid surface free energy of water in Cassie and Wenzel wetting states on rugged solid surfaces at the nanometer scale. Langmuir. 2011;27:637–645.

[46] Savoy ES, Escobedo A. Simulation study of free-energy barriers in the wetting transition of an oily fluid on a rough surface with reentrant geometry. Langmuir. 2012;28:16080–16090.

[47] Giacomello A, Meloni S, Chinappi M, Casciola M. Cassie–Baxter and Wenzel states on a nanostructured surface: phase diagram, metastabilities, and transition mechanism by atomistic free energy calculations. Langmuir. 2012;28:10764–10772.

[48] Leroy F, Mueller-Plathe F. Can continuum thermodynamics characterize Wenzel wetting states of water at the nanometer scale. J Chem Theory Comput. 2012;8:3724–3732.

[49] Leroy F, Santos DJVAd, Muller-Plathe F. Interfacial excess free energies of solid–liquid interfaces by molecular dynamics simulation and thermodynamic integration. Macromol Rapid Commun. 2009;30:864–870.

[50] Todorov IT, Smith W, TK, Dove MT. DL_POLY_3: new dimensions in molecular dynamics simulations via massive parallelism. J Mat Chem. 2006;16:1911–1918.

[51] Berendsen HJC, Grigera JR, Straatsma P. The missing term in effective pair potentials. J Phys Chem. 1987;91:6269–6271.

[52] Miyamoto S, Kollman A. Settle: an analytical version of the SHAKE and RATTLE algorithm for rigid water models. J Comp Chem. 2004;13:952–962.

[53] Werder T, Walther JH, Jaffe RL, Halicioglu T, Koumoutsakos P. On the water–carbon interaction for use in molecular dynamics simulations of graphite and carbon nanotubes. J Phys Chem B. 2003;107:1345–1352.

[54] Darden T, York D, Pedersen L. Particle mesh Ewald: an $N\log(N)$ method for Ewald sums in large systems. J Chem Phys. 1993;98 :10089–10092.

[55] Park JH, Aluru R. Temperature-dependent wettability on a titanium dioxide surface. Mol Simul. 2009;35:31.

[56] Ruijter MJd, Blake TD, Coninck JD. Dynamic wetting studied by molecular modeling simulations of droplet spreading. Langmuir. 1999;15:7836–7847.

[57] Thomas JA, McGaughey JH. Effect of surface wettablility on liquid density, structure, and diffusion near a solid surface. J Chem Phys. 2007;126:034707.

[58] Lee JB, Gwon HR, Lee SH, Cho M. Wetting transition characteristics on microstructured hydrophobic surfaces. Mater Trans. 2010;51:1709–1711.

[59] Yong X, Zhang T. Nanoscale wetting on groove-patterned surfaces. Langmuir. 2009;25:5045–5053.

[60] Yoshimitsu Z, Nakajima A, Watanabe T, Hashimoto K. Effects of surface structure on the hydrophobicity and sliding behavior of water droplets. Langmuir. 2002;18:5818–5822.

[61] Ishino C, Okumura K, Quere D. Wetting transitions on rough surfaces. Europhys Lett. 2004;68:419–425.

[62] Jeong W-J, Ha MY, Yoon HS, Ambrosia M. Dynamic behavior of water droplets on solid surfaces with pillar-type nanostructures. Langmuir. 2012;28:5360–5371.

[63] Erbil HY, Cansoy E. Range of applicability of the Wenzel and Cassie–Baxter equations for superhydrophobic surfaces. Langmuir. 2009;25:14135–14145.

[64] Dettre RH, Johnson RE. Contact Angle Hysteresis II. Contact Angle measurements on rough surfaces. Adv Chem. 1963;43:136–144.